Reflectance properties of two-dimensional sonic band-gap crystals

L. Sanchis[a] and F. Cervera
Centro Tecnológico de Ondas, Unidad Asociada de Investigación (CSIC), Edificio de Institutos II, Universidad Politécnica de Valencia, Avenida de los Naranjos s/n, 46022 Valencia, Spain

J. Sánchez-Dehesa[b]
Departamento de Física Teórica de la Materia Condensada, Facultad de Ciencias (C-V), Universidad Autónoma de Madrid, 28049 Madrid, Spain

J. V. Sánchez-Pérez, C. Rubio, and R. Martínez-Sala
Centro Tecnológico de Ondas, Unidad Asociada de Investigación (CSIC), Edificio de Institutos II, Universidad Politécnica de Valencia, Avenida de los Naranjos s/n, 46022 Valencia, Spain

(Received 23 August 2000; accepted for publication 12 March 2001)

An analysis of the reflectance of sonic band-gap crystals consisting of square arrays of rigid cylinders in air is presented. The standing wave formed in front of the structures is studied both experimentally and theoretically. Experiments have been performed with a mobile robotized microphone that obtains pressure maps on the plane perpendicular to the axes of the cylinders. Enhancements of the standing wave ratio (SWR) are observed in frequency regions where attenuation bands appear in zero-order transmission experiments. Also, the SWR presents oscillations that can be related to the finite dimension of the structure (Fabry–Perot effect). Both features are well described by calculations based on a double-scattering approach. © *2001 Acoustical Society of America.* [DOI: 10.1121/1.1369784]

PACS numbers: 43.20.Fn, 43.20.Ks, 43.20.Ye [ANN]

I. INTRODUCTION

The existence of frequency regions where the propagation of electromagnetic waves is forbidden was predicted in certain structures having a periodic modulation of the dielectric function.[1,2] The structures that exhibit such behavior are called photonic-band-gap (PBG) materials. The underlying theory has been applied to other types of waves like sound or elastic waves and the corresponding structures are called sonic-band-gap (SBG) or elastic-band-gap (EBG) materials. Great theoretical effort has been put into the study of these kinds of waves.[3–6] Most of the works calculated the acoustic band structure of infinite crystal using the plane-wave expansion method. Recently, other approaches based on a variational method[7] and a Korringa–Khon–Rostoker method[8] have been developed. On the other hand, finite systems have been studied by the transfer-matrix method[9] and multiple-scattering theory.[10] In this work we use multiple-scattering theory to study our finite samples. In our approach each scatterer is characterized by its scattered pressure, which links the diffracted pressure field to the incoming one. Our procedure is a simplified version of the one employed in Ref. 11, which uses a rigorous multiple-scattering theory to study light scattering by dielectric cylinders. We will see that this simplified approach, which takes up to double-scattering events, reproduces the experiments fairly well.

Most experimental work on SBG structures reports zero-order attenuation spectra.[7,12,13] A recent paper by Torres *et al.*[14] shows nice pictures of Bloch waves on a liquid having wave velocity modulation. In the same spirit we have developed an experimental setup which permits the measurement of pressure patterns in the plane where the two-dimensional arrays of scatterers are deployed.

Making use of both theoretical and experimental tools, our goal in this work is to study the reflectance properties of SBG crystals formed by two-dimensional arrays of rigid rods in air. Those properties will be inferred from the study of the partial standing wave formed in front of the SBG structure. As we discuss below, the method of pressure measurement effectively detects a full standing wave whose standing wave ratio (SWR) allows the characterization of some features in the acoustic band structure. Also, the comparison with our model based on a multiple-scattering approach facilitates such analysis.

II. THEORETICAL APPROACH

A. Sound scattering by an ensemble of rigid cylinders in single-scattering approach

Let us first compute the scattering of a sound plane wave, with frequency ω, by a cylinder of radius R_0 placed at the origin of coordinates. The incident wave travels in a direction perpendicular to the cylinder's axis (i.e., along the positive X axis) and impinges on a cylinder infinite along the Z axis. If we assume a temporal dependence $e^{-i\omega t}$, the wave can be expressed as

$$P^{\text{incid}} = e^{ikx} = e^{ikr\cos\theta} = \sum_{s=-\infty}^{s=\infty} i^s J_s(kr) e^{is\theta}, \tag{1}$$

where k is the wave number ($k=2\pi/\lambda$) and J_s is the Bessel function of the first kind and order s. The scattered wave takes the form

[a]Electronic mail: lsanchis@fis.upv.es
[b]Electronic mail: jose.sanchezdehesa@uam.es

$$P^{\text{scatt}}=\sum_{s=-\infty}^{s=\infty} A_s H_s(kr)e^{is\theta}, \tag{2}$$

where H_s is the Hankel function of the first kind and order s with the superscript (1) omitted for simplicity; $H_s(z)=J_s(z)+iY_s(z)$, $Y_s(z)$ is the Bessel function of the second kind and order s. The coefficients A_s are calculated by applying the boundary condition on the cylinder's surface.

If we assume a rigid cylinder, the radial velocity of the air particles at the surface must be zero. This velocity is generated by the combination of the plane wave and the scattered wave. Since the velocity is proportional to the pressure gradient, this boundary condition is

$$\frac{\partial}{\partial r}[P^{\text{inc}}+P^{\text{scatt}}]_{r=R_0}=0. \tag{3}$$

After an easy calculation, the coefficients are

$$A_s=\frac{-i^s(J_{s-1}(kR_0)-J_{s+1}(kR_0))}{(H_{s-1}(kR_0)-H_{s+1}(kR_0))}. \tag{4}$$

The total pressure at any point on the XY plane is the sum of the scattered wave and the incident wave

$$P=P^{\text{inc}}+P^{\text{scatt}}. \tag{5}$$

Now, if we consider that the wave is scattered not by a single cylinder but by an ensemble, a scattered wave is generated on every cylinder and, therefore, to obtain the net pressure we have to add the waves of all cylinders at any point of the XY plane. This is a single-scattered approach since it involves the scattered pressure originated in each cylinder by just the incident wave arriving on it. Let us assume that the jth cylinder is placed at the point (x_j, y_j); so, if we take the phase origin at $x=0$, when the plane wave reaches this cylinder its phase will be kx_j, and the corresponding scattered pressure at this point must be the same as the one calculated above multiplied by the phase factor $\exp(ikx_j)$

$$P_j^{\text{scatt}}=e^{ikx_j}\sum_{s=-\infty}^{s=\infty} A_s H_s(kr_j)e^{is\theta_j}. \tag{6}$$

Therefore, the total pressure at the point (x, y) takes the form

$$\begin{aligned}P(x,y)&=P^{\text{inc}}+\sum_{j=1}^{N} P_j^{\text{scatt}}\\&=e^{ikx}+\sum_{j=1}^{N} e^{ikx_j}\sum_{s=-\infty}^{s=\infty} A_s H_s(kr_j)e^{is\theta_j},\end{aligned} \tag{7}$$

N being the number of cylinders ($j=1, \ldots, N$).

We must keep in mind that this pressure field is related to the system of coordinates of each cylinder j

$$\begin{aligned}r_j&=\sqrt{(x-x_j)^2+(y-y_j)^2},\\\theta_j&=\arcsin((y-y_j)/r_j).\end{aligned} \tag{8}$$

This approach usually works well in systems where the scatterers are distant enough from each other; in other words, when the fraction of volume occupied by the cylinders is small.

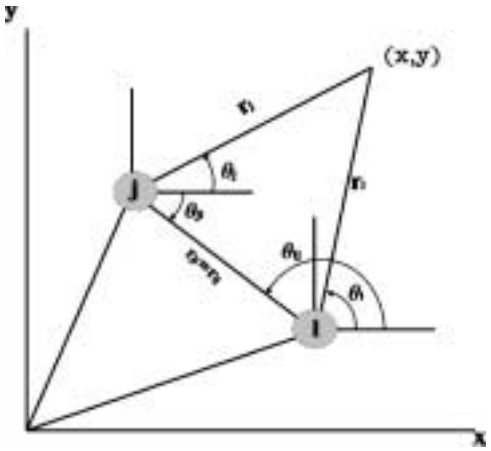

FIG. 1. Notation used for a change of coordinate system between cylinder jth and lth. They are placed at the points (x_j, y_j) and (x_l, y_l).

B Sound scattering by an ensemble of cylinders with double-scattering term

Now, consider cylinder jth and lth shown in Fig. 1. As we mentioned before, the field generated by the plane wave on the jth cylinder is

$$P_j=e^{ikx_j}\sum_{s=-\infty}^{s=\infty} A_s H_s(kr_j)e^{is\theta_j}. \tag{9}$$

Using Graf's formula[15] for the Hankel function, we can express the term $H_s(kr_j)e^{is\theta_j}$ in the lth coordinate system

$$H_s(kr_j)e^{is\theta_j}=\sum_{q=-\infty}^{q=\infty} e^{[i(s-q)\theta_{lj}]}H_{q-s}(kr_{lj})J_q(kr_l)e^{iq\theta_l}. \tag{10}$$

The pressure scattered by the jth cylinder in the system of coordinates of the lth cylinder is

$$P_{jl}=\sum_{s=-\infty}^{s=\infty} A_s e^{ikx_j}\sum_{q=-\infty}^{q=\infty} e^{[i(s-q)\theta_{lj}]}H_{q-s}(kr_{lj})J_q(kr_l)e^{iq\theta_l}. \tag{11}$$

The field generated at the lth cylinder produced by the wave scattered by the jth cylinder can be written in the following form:

$$PP_{jl}=\sum_{s=-\infty}^{s=\infty} A_{jls} H_s(kr_l)e^{is\theta_l}. \tag{12}$$

If we apply the boundary condition on the lth cylinder

$$\frac{\partial}{\partial r_l}[P_{jl}+PP_{jl}]_{r_l=R_o}=0, \tag{13}$$

$$\begin{aligned}\frac{\partial}{\partial r_l}\Bigg[&\sum_{s=-\infty}^{s=\infty} A_s e^{ikx_j}\sum_{q=-\infty}^{q=\infty} e^{[i(s-q)\theta_{lj}]}H_{q-s}(kr_{lj})J_q(kr_l)e^{iq\theta_l}\\&+\sum_{s=-\infty}^{s=\infty} A_{jls} H_s(kr_l)e^{is\theta_l}\Bigg]_{r_l=R_o}=0.\end{aligned} \tag{14}$$

Making use of the relations between the partial derivatives of the Bessel and Hankel functions, the last equation takes the form

$$A_s e^{ikx_j} \sum_{q=-\infty}^{q=\infty} e^{[i(s-q)\theta_{lj}]} H_{q-s}(kr_{lj})(J_{q-1}(kR_o) - J_{q+1}(kR_o)) e^{iq\theta_l} + A_{jls}(H_{s-1}(kR_o) - H_{s+1}(kR_o)) e^{is\theta_l} = 0. \tag{15}$$

Now it is possible to find the coefficients A_{jls}

$$A_{jls} = \frac{A_s e^{ikx_j} \Sigma_{q=-\infty}^{q=\infty} e^{[i(s-q)\theta_{lj}]} H_{q-s}(kr_{lj})(J_{q+1}(kR_0) - J_{q-1}(kR_0))}{(H_{s-1}(kR_0) - H_{s+1}(kR_0))} e^{i(q-s)\theta_l}. \tag{16}$$

We can repeat the same process, but this time the *l*th cylinder is the one that induces the scattered wave on the *j*th. In this case the coefficients are

$$A_{ljs} = \frac{A_s e^{ikx_l} \Sigma_{q=-\infty}^{q=\infty} e^{[i(s-q)\theta_{jl}]} H_{q-s}(kr_{jl})(J_{q+1}(kR_0) - J_{q-1}(kR_0))}{(H_{s-1}(kR_0) - H_{s+1}(kR_0))} e^{i(q-s)\theta_j}. \tag{17}$$

It is clear that $j=l$ makes no sense regarding the coefficients A_{ljs}. Therefore, the coefficients can be cast in the following form:

$$A_{ljs} = (1-\delta_{lj}) \frac{A_s e^{ikx_l} \Sigma_{q=-\infty}^{q=\infty} e^{[i(s-q)\theta_{jl}]} H_{q-s}(kr_{jl})(J_{q+1}(kR_0) - J_{q-1}(kR_0))}{(H_{s-1}(kR_0) - H_{s+1}(kR_0))} e^{i(q-s)\theta_j}, \tag{18}$$

where δ_{lj} is the Kronecker delta ($\delta_{lj}=1$ if $l=j$ and $\delta_{lj}=0$ if $l \neq j$). The pressure induced on the *j*th cylinder by the *l*th is

$$PP_{lj} = \sum_{s=-\infty}^{s=\infty} A_{ljs} H_s(kr_j) e^{is\theta_j}. \tag{19}$$

So, the pressure field produced by a finite number of cylinders, *N*, due to the double-scattering process is

$$PP^{\text{scatt}} = \sum_{l=1}^{N} \sum_{j=1}^{N} \sum_{s=-\infty}^{s=\infty} A_{ljs} H_s(kr_j) e^{is\theta_j}. \tag{20}$$

This is the multiple-scatter term employed in our calculation.

Finally, the pressure at any point (x, y) will be the sum of all contributions

$$\begin{aligned} P(x,y) &= P^{\text{inc}} + P^{\text{scatt}} + PP^{\text{scatt}} \\ &= e^{ikx} + \sum_{j=1}^{N} e^{ikx_j} \sum_{s=-\infty}^{s=\infty} A_s H_s(kr_j) e^{is\theta_j} \\ &\quad + \sum_{l=1}^{N} \sum_{j=1}^{N} \sum_{s=-\infty}^{s=\infty} A_{ljs} H_s(kr_j) e^{is\theta_j}. \end{aligned} \tag{21}$$

Notice that the summations over *j* and *l* permit the analysis of any arrangement of cylinders, either ordered or disordered. Here, we are concerned with ordered structures.

Let us stress that our approach cuts the expansion procedure of Twersky[16] after the double-scattering term. Our simplified approach is justified by the agreement with experimental results as described below.

III. EXPERIMENTS

The experiments have been performed in an anechoic chamber of $8 \times 6 \times 3$-m^3 size. As a sound source we used a speaker placed at the focus of a parabolic reflector. The reflector is employed to collimate the beam. Nevertheless, the distance between the source and sample is not enough to produce full plane-wave fronts when the sound reaches the sample.

With the aim of obtaining pressure maps on the plane perpendicular to the cylinder's axis, we have developed a computer-controlled automatic positioning system (called robot for short) capable of sweeping the microphone through a grid of measuring points located in a plane. The movement along each *X*- or *Y*-axis is accomplished by means of steeper motors with a maximum resolution of 0.25 mm per step. The maximum length of each axis is 1800 mm. Nevertheless, larger distances can be explored by hand relocation of the whole frame of the robot. Sound-pressure measurements are automatically taken by means of a B&K 2144 frequency analyzer controlled by a computer through a general purpose interface bus (GPIB) interface. At each grid point the microphone samples the sound with a sampling frequency of 15 kHz. Afterwards the analyzer makes the fast Fourier transform (FFT) of such data and produces the corresponding pressure spectrum with a resolution of 8Hz. Frequencies below 6.4 kHz are well described in the spectra. A total of 256 spectra has been taken to generate an averaged spectrum, which is the one finally assigned to that grid point. The total measuring time in one point is 10 s. As a result we obtain at each point, and for a given frequency, the root-mean-squared (rms) pressure, $P_{\text{rms}}(x,y)$. In order to put it in decibels we used a reference pressure $P_{\text{ref}} \equiv 20$ μPa; in other words, $L_{\text{exp}}(x,y) = 20 \log_{10}(P_{\text{rms}}(x,y)/P_{\text{ref}})$. The total time employed to elaborate a pressure map with 400 grid points, like the ones shown here, is about 7 h.

Our SBG crystals are built up by hanging cylindrical rods on a frame which has the crystal symmetry. Here, we have studied square arrays of hollow aluminum rods of $R_0 = 2$ cm radius put in a square lattice with 11 cm of lattice constant, *a*. The fraction of volume occupied by the cylinders *f* is quite small: $f = \pi R_0^2/a^2 = 0.104$. It has been shown previously[17] that this structure does not possess a full acoustic band gap.

In Fig. 2 we show the two samples under study. They were constructed along the *X* axis, the incident sound direction, in order to represent the two high-symmetry directions in the Brillouin zone; i.e., the ΓX direction [Fig. 2(a)] and

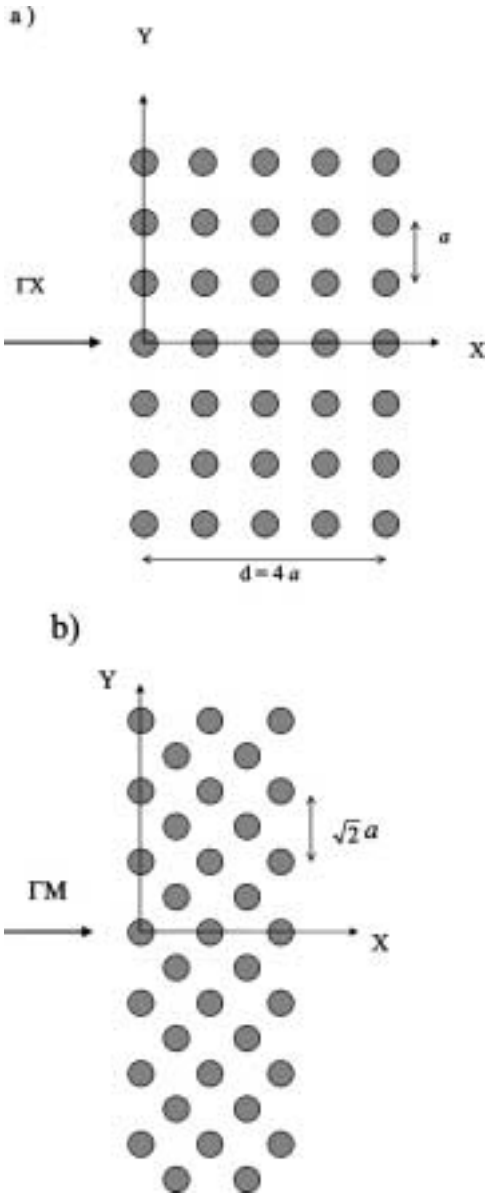

FIG. 2. (a) Geometry of the sample used to study the scattering of sound waves incident along the Γ*X* direction. (b) Sample employed to study sound waves along the Γ*M* direction. The incident direction is always from left to right in the figures.

Γ*M* direction [Fig. 2(b)], respectively. Both structures have five rows of cylinders so as to have short computational times, and to make for an easier comparison. We choose them as test materials to study their properties in reflectance by using our experimental setup.

IV. RESULTS AND DISCUSSION

The structures under study have been analyzed previously by using zero-order transmission experiments, and the following results were obtained: (1) along the Γ*X* direction an attenuation band appears[18] in the frequency region (1260–1750 Hz); (2) along the Γ*M* direction the attenuation band measured covers the region (1900–2500 Hz). When compared to the acoustic band structure calculated by a variational method one finds that attenuation along Γ*X* is fairly well explained by the gap existing at the region (1204–1764 Hz). On the contrary, along the Γ*M* no gap was found in the band calculation. The origin of the attenuation along this direction is twofold. One is the existence of one deaf band;[7] i.e., a band that is not coupled with the incident sound for reasons of symmetry. The other is the possible energy transfer to Bragg waves of higher order when the sound leaves the sample. In what follows we will see how these effects are shown in our experiments and by our multiple scattering calculation. First, we analyze pressure maps. Afterwards, the study of the standing wave observed in front of the structure will give us further confirmation of the SBG crystal properties inferred from the transmission experiments.

A. Pressure maps

The pressure, $P(x,y)$, has been calculated by our double-scattering approach (see Sec. II) at different frequencies. The sums to the orders of Hankel functions, *s* or *q*, have been truncated to five terms. This truncation is justified due to the fast decreasing of the coefficient's modulus. Thus, for example, at 2720 Hz, $|A_0|/|A_3| \approx 140$. On the other hand, to reduce the computational time the double-scattering term, Eq. (20), is calculated by using just first-neighbors interaction; i.e., $A_{ljs}=0$ if $r_{lj} > \sqrt{2}a$.

To compare with experiments we define a theoretical RMS-pressure, $P^2_{\text{theo}}(x,y)=\frac{1}{2}PP^*=\frac{1}{2}|P(x,y)|^2$, which is the average squared pressure at each point.

Therefore, the pressure in decibels is

$$L_{\text{theo}}(x,y)=20\ \log_{10}(|P(x,y)|/\alpha), \tag{22}$$

where α is an adjustable parameter that takes into account that the incident pressure is not unity in the experiments. In particular, we will present here results for two relevant frequencies; both are in regions where attenuation bands are observed.

Figure 3 shows the calculated pressure pattern at 1600 Hz for the sample constructed along the Γ*X* direction [see Fig. 2(a)]. It can be observed how the pressure decreases as the wave penetrates inside the structure. This behavior is well explained by the fact that the frequency is inside the existing acoustic gap along this direction. Both low transmission and high reflectance are observed along the incident direction, as is shown in Fig. 3. On the other hand, Fig. 4 plots the map obtained at 2540 Hz for the sample constructed along the Γ*M* direction. In comparison with the previous result, we now notice how the pressure takes nonzero values at angles tilted with respect to the incident direction and in the lateral sides of the structure. In this case the attenuation measured in the forward direction is due to an energy transfer to other directions; i.e., other than the collinear between source and microphone.

In Fig. 5 we compare pressure maps calculated and measured for the same sample and at the same frequency as in Fig. 3. The area represented in front of the structure is $x \in [-0.985\text{ m}, -0.485\text{ m}]$, $y \in [-0.160\text{ m}, 0.160\text{ m}]$. This plot shows that both experiment and theory display periodic high- and low-pressure levels, which clearly define standing waves that are in good qualitative agreement.

Figure 6 compares the measured values (squares) with the predictions of the model inside the region (−0.985 m,

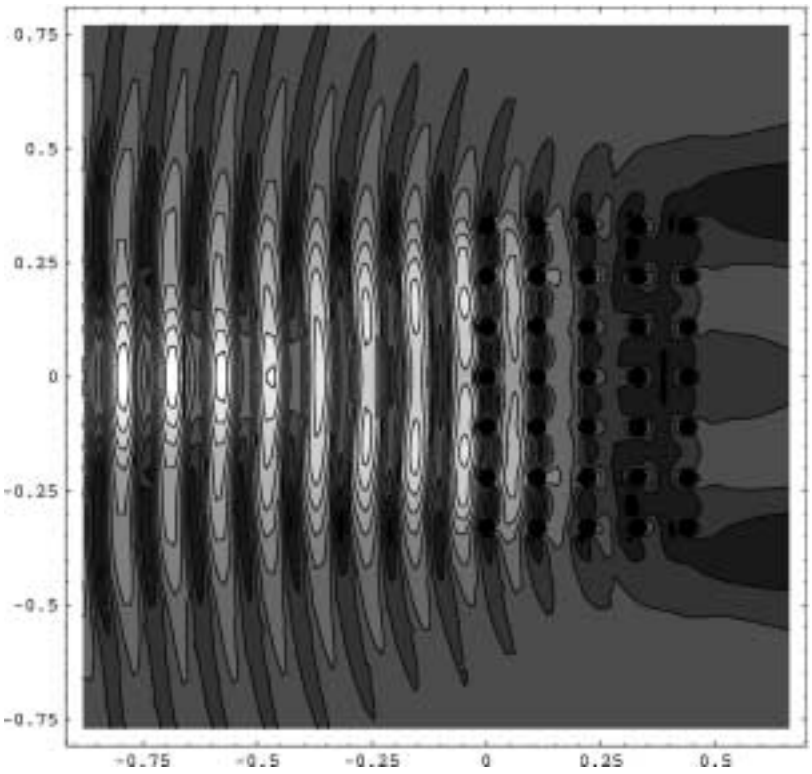

FIG. 3. Double-scattering calculation of the mean-square pressure pattern at 1600 Hz for the sample along the ΓX direction [see Fig. 2(a)].

-0.485 m) along the X axis. The continuous line represents the function $L_{\text{theo}}(x,y=0)$ in Eq. (22) with $\alpha=0.004$. We fitted the theoretical curve so that experimental maxima and minima were always above and below, respectively, the calculated ones. An improved fitting could have been done if our calculations had taken into account the fact that the incident sound probably does not have a plane-wave front when it reaches the structures. This effect will be discussed further in the next subsection.

B. Standing wave ratio

If we consider that an incident sound wave with unit pressure amplitude impinges on the SBG crystal, it will be

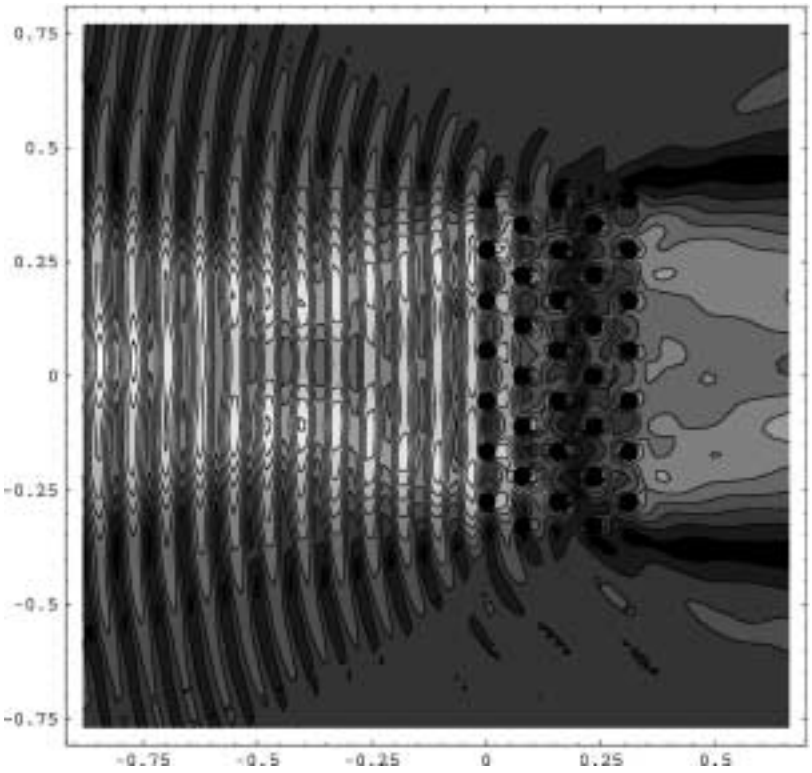

FIG. 4. Double-scattering calculation of the mean-square pressure pattern at 2540 Hz for the sample along the ΓM direction [see Fig. 2(b)].

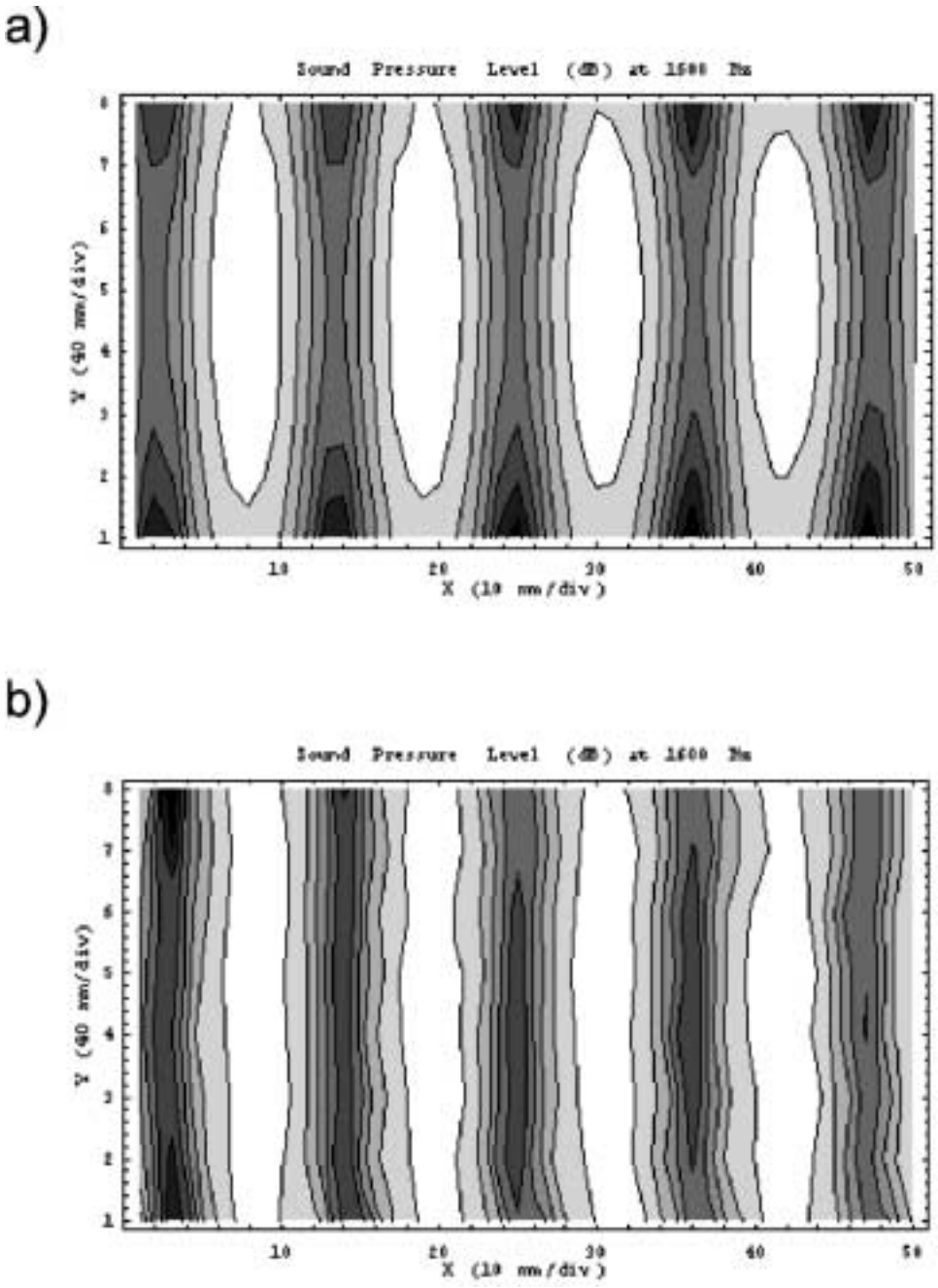

FIG. 5. Comparison between the mean-square pressure levels calculated (a) and measured (b) for the sample along the ΓX direction at 1600 Hz. The area represented in front of the sample is $(-0.985$ m, -0.485 m$)\times(-0.160$ m, 0.160 m), along the x- and y-axis, respectively. The scale numbered the grid points employed in the plot.

partially reflected. The net pressure in front of the crystal is the superposition of the incident and reflected wave

$$\cos(kx-\omega t)+R\ \cos(-kx-\omega t)$$
$$=A(x)\cos(-\omega t-\varphi(x)), \tag{23}$$

where R is the reflection coefficient, $\varphi(x)$ is a phase angle which is of no concern here, and $A(x)=\sqrt{1+2R\ \cos 2kx+R^2}$. Only for $R=\pm 1$ is a full standing wave formed. For the general case $R\neq\pm 1$ the sum of the incoming traveling wave and the reflected wave is a partial standing wave. If we explore the wave with a microphone, as we have done, we are, in fact, measuring its mean square pressure, $\overline{P^2}$. In other words, we are measuring $A(x)$, which ranges (if $R>0$) from a maximum value $(1+R)$ at antinode positions $kx=0+n\pi$, to a minimum value $(1-R)$ at node position $kx=\pi/2+n\pi$. The standing wave ratio is defined by[19]

$$\frac{\overline{P^2}_{\max}}{\overline{P^2}_{\min}}=\frac{(1+R)^2}{(1-R)^2}=\mathrm{SWR}^2. \tag{24}$$

Experimentally, to obtain the SWR it is better to work in terms of rms-pressures

$$\mathrm{SWR}_{\exp}=L_{P\max}-L_{P\min}$$
$$=10\ \log_{10}(P_{\max}/P_{\mathrm{ref}})^2-10\ \log_{10}(P_{\min}/P_{\mathrm{ref}})^2$$
$$=20\ \log_{10}(P_{\max}/P_{\min}). \tag{25}$$

In this equation $L_{P\min}$ and $L_{P\max}$ are the rms-pressure levels measured in decibels, P_{ref} is an arbitrary value (see Sec. III), and $P_{\max}$ and $P_{\min}$ are the maximum and minimum values of

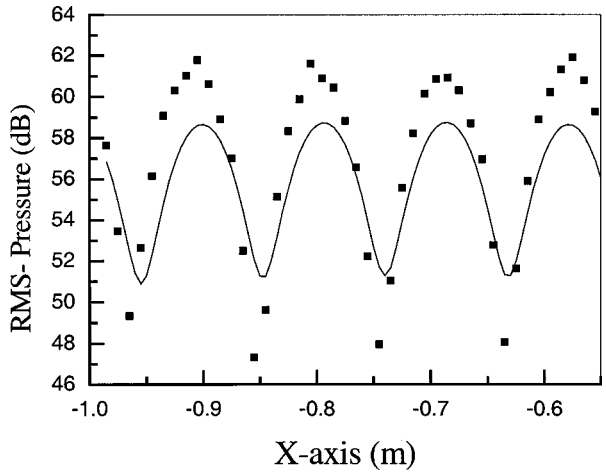

FIG. 6. Comparison between the effective pressures measured (symbols) and calculated (solid line) for the sample constructed along the ΓX direction at 1600 Hz. The data represented are in the region (-0.985 m, -0.485 m) along the x axis.

the root time-averaged pressures, respectively.

With regards to theoretical calculation, the SWR can be calculated using the following formula:

$$\mathrm{SWR}_{\mathrm{theo}} = 20\ \log_{10}(|P_{\max}|/|P_{\min}|). \tag{26}$$

Figures 7 and 8 show the SWRs along the two high-symmetry directions: ΓX and ΓM, respectively. The thick solid lines represent the measurements, while dotted lines define the calculations using the theory described in Sec. II. On the other hand, to evaluate the effect associated with a possible nonplanar wavefront, a phase mismatch between the cylinders in the planes perpendicular to the incident wave has been introduced in the model: the phase factors are considered to have the form $e^{ik|\mathbf{R}_{\mathrm{source}}-\mathbf{r}_j|}$ instead of $\exp(ikx_j)$, where $\mathbf{r}_j=(x_j,\ y_j)$ is the position vector of the cylinder j, and $\mathbf{R}_{\mathrm{source}}$ is the position of a line source at a distance L in front of the sample; $\mathbf{R}_{\mathrm{source}}=(-L,0)$. The thin solid lines in Figs. 7 and 8 represent the calculations for this cylindrical wavefront with a fitted value $L=10a$.

When the sound wave impinges the structure along the ΓX direction (see Fig. 7), the SWR measured (thick solid line) show an enhancement in the very same frequency region where the first gap appears in the acoustic band structure. The lack of states available to sound transmission produces a large reflectance R and, consequently, explains the SWR increasing. With regard to the oscillations observed, they are related to the resonances associated with the finite thickness of the SBG crystal (Fabry–Perot resonances). The frequency of these resonances is determined by $kd=m\pi$, $m=1,2,\ldots$, $d=4a=0.44$ m being the thickness of the sample constructed along this direction [see Fig. 2(a)]. From the oscillation period, $\Delta\omega$, it would be possible to obtain the sound velocity inside the sonic crystal (SC), c_{SC}, through the formula $c_{\mathrm{SC}}=\Delta\omega d/\pi$. Nevertheless, since the period measured changes with frequency (its values are in the range 222–355 Hz), a frequency-dependent sound velocity must be considered instead. The study of this magnitude, which impinges on the broad problem of homogenization, requires the analysis of more structures and detailed calculations on their corresponding acoustic bands for comparison. Such a task is beyond the scope of this work. The comparison with the SWR resulting from our double-scattering model is qualitatively good, although both calculations (i.e., plane and cylindrical wavefronts, respectively) define the gap shifted with respect to the measurements and the band structure calculation. This disagreement mainly comes from the fact that we didn't include all the multiple-scattering terms as they are in the acoustic band calculation. Furthermore, the result for the case of a cylindrical wavefront predicts a smaller gap.

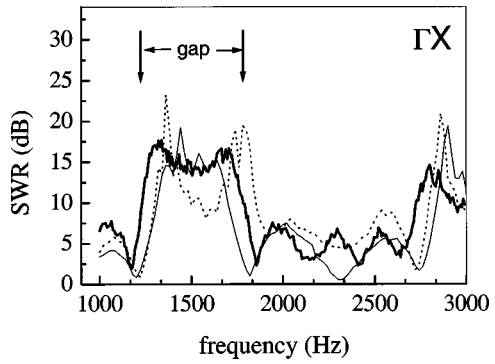

FIG. 7. Frequency dependence of the standing wave ratio (SWR) (in dB) measured (thick solid line) and calculated for the sample along the ΓX direction. The dotted line represents the calculated results for an incoming sound plane wave. The thin solid line shows the corresponding ones calculated with an incident sound with a cylindrical shape (see the text).

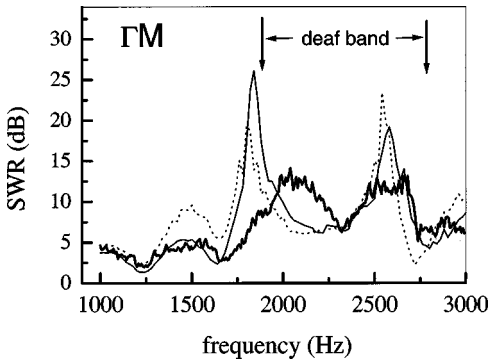

FIG. 8. Frequency dependence of the SWR (in dB) measured (thick solid line) and calculated for the structure along the ΓM direction. The dotted line represents the calculated results for an incoming sound plane wave. The thin solid line shows the corresponding ones calculated with an incident sound with a cylindrical shape (see the text).

When the sound is incident along the ΓM direction (see Fig. 8) we notice an SWR enhancement in the region (1800–2700 Hz), though no gap appears in the acoustic band structure calculated along this direction. Now, the origin of large SWR values is associated with the existence of a deaf band that goes from 1878 Hz up to 2798 Hz. This band, ideally uncoupled, weakly couples with the exciting sound and produces large reflectance values. The multiple-scattering calculations are also in qualitatively good agreement and reproduce most of the features observed. Again, the theoretical frequencies at which the SWR enhances are shifted (now to lower frequencies) compared to the experimental ones and to the ones deduced from band structure. Regarding the Fabry–Perot oscillations, its period is now larger since the slab thickness is smaller, $d=4a/\sqrt{2}=0.31$ m. These oscilla-

tions are well reproduced by our models. In fact, we observe that the results with the cylindrical wavefront give a better account of the SWR amplitude. This effect leads us to conclude that phase mismatch plays a role and has to be included in improved models based on the multiple-scattering approaches.

V. SUMMARY

In this work we have studied the standing wave formed in front of a SBG crystal when a sound wave impinges on it. The crystals analyzed consist of two-dimensional arrays of rigid cylinders in air. Experiments were conducted in an free-echo chamber by using a new experimental setup based on a computer-controlled automatic positioning system which is able to obtain the effective pressure pattern on the plane perpendicular to the cylinder axis. On the other hand, we have used a theoretical approach based on a multiple-scattering algorithm, which takes into account up to double-scattering events. The comparison between theory and experiments has allowed us to obtain intrinsic properties of the SBG crystal. In particular, we have shown that gaps and uncoupled bands can be characterized in the SWR of the standing wave. Moreover, the finite thickness of our SBG structures along the sound propagation direction produces Fabry–Perot-type resonances that were detected as oscillations in the SWR.

ACKNOWLEDGMENTS

This work has been supported by the Comisión Interministerial de Ciencia y Tecnología of Spain, Contract No. MAT00-1670-C04. We thank F. Meseguer for his continuous support. Also, we thank D. Caballero, R. Llopis, and D. López for their comments and suggestions. We acknowledge the computational help provided by the Centro de Computación Científica at the Universidad Autonoma de Madrid.

[1] E. Yablonovitch, ''Inhibited spontaneous emission in solid state physics and electronics,'' Phys. Rev. Lett. **58**, 2059–2062 (1987).
[2] S. John, ''Strong localization of photons in certain disordered structures,'' Phys. Rev. Lett. **58**, 2486–2489 (1987).
[3] L. Flax, L. R. Dragonette, and H. Uberall, ''Theory of elastic resonance excitation by sound scattering,'' J. Acoust. Soc. Am. **63**, 723–731 (1978).
[4] M. M. Sigalas and E. N. Economou, ''Elastic and acoustic band structure,'' J. Sound Vib. **158**, 377–382 (1992).
[5] M. S. Kushwaha, P. Halevi, L. Dobrzynski, and B. Djafrari-Rouhani, ''Acoustic band structure of periodic elastic composites,'' Phys. Rev. Lett. **71**, 2022–2025 (1993).
[6] E. N. Economou and M. Sigalas, ''Classical wave propagation in periodic structures,'' Phys. Rev. B **48**, 13434–13438 (1993).
[7] J. V. Sánchez-Pérez, D. Caballero, R. Martínez-Sala, C. Rubio, J. Sánchez-Dehesa, F. Meseguer, J. Llinares, and F. Gálvez, ''Sound attenuation by a two-dimensional array of rigid cylinders,'' Phys. Rev. Lett. **80**, 5325–5328 (1998).
[8] M. Kafesaki and E. N. Economou, ''Multiple scattering theory for 3D periodic acoustic composites,'' Phys. Rev. B **60**, 11993–11999 (1999).
[9] M. M. Sigalas and N. Economou, ''Attenuation of multiple scattered sound,'' Europhys. Lett. **36**, 241–246 (1996).
[10] Zhen Ye, ''Acoustic localization in bubbly liquid media,'' Phys. Rev. Lett. **80**, 3503–3506 (1998).
[11] D. Felbacq, G. Tayeb, and D. Maystre, ''Scattering by a random set of parallel cylinders,'' J. Opt. Soc. Am. A **11**, 2526–2538 (1994).
[12] F. R. Montero de Espinosa, E. Jiménez, and M. Torres, ''Ultrasonic band gap in a periodic two-dimensional composite,'' Phys. Rev. Lett. **80**, 1208–1211 (1998).
[13] W. M. Robertson and W. F. Rudy, III, ''Measurement of acoustic stop bands in two-dimensional periodic scattering arrays,'' J. Acoust. Soc. Am. **104**, 694–699 (1998).
[14] M. Torres, J. P. Adrados, and F. R. Montero de Espinosa, ''Visualizacion of Bloch waves and domain walls,'' Nature (London) **398**, 114–115 (1999).
[15] E. T. Wittaker and G. N. Watson, *A Course of Modern Analysis* (Cambridge University Press, Cambridge, 1965), p. 429.
[16] V. Twersky, ''On scattering of waves by random distributors,'' J. Math. Phys. **3**, 700–715 (1962).
[17] See Fig. 4 in Ref. 7.
[18] See Fig. 1 in Ref. 7.
[19] D. H. Towne, *Wave Phenomena* (Dover, New York, 1988), pp. 49–51.